Solar Physics manuscript No.
(will be inserted by the editor)

B. Inhester[1], L. Feng[1,2], T. Wiegelmann[1]

Segmentation of loops from coronal EUV images

Submitted July 31, 2007 as a contribution to the topical issue on image processing

Abstract We present a procedure which extracts bright loop features from solar EUV images. In terms of image intensities, these features are elongated ridge-like intensity maxima. To discriminate the maxima, we need information of the spatial derivatives of the image intensity. Commonly, the derivative estimates are strongly affected by image noise. We therefore use a regularized estimation of the derivative which is then used to interpolate a discrete vector field of ridge points(ridgels) which are positioned on the ridge center and have the intrinsic orientation of the local ridge direction. A scheme is proposed to connect ridgels to smooth, spline-represented curves which fit the observed loops. Finally, a half-automated user interface allows to merge or split, eliminate or select loop fits obtained form the above procedure. In this paper we apply our tool to one of the first EUV images observed by the SECCHI instrument on board the recently launched STEREO spacecraft. We compare the extracted loops with projected field lines computed from almost simultaneously taken magnetograms measured by the MDI/SOHO Doppler imager using a linear force-free field model. This comparison allows to verify faint and spurious loop connections produced by our segmentation tool and it also helps to prove the quality of the magnetic field model where well identified loop structures comply with field line projections. We also discuss further potential applications of our tool such as loop oscillations and stereoscopy.

1 Introduction

Solar EUV images offer a wealth of information about the structure of the solar chromosphere, transition region and corona. Moreover, these structures are in continuous motion so that the information collected by EUV images of the Sun is enormous. For many purposes this information must be reduced. A standard task for many applications, e.g., for the comparison with projected field lines computed from a coronal magnetic field model or for tie-point stereoscopic reconstruction, requires to extract the shape of bright loops from these images.

Solar physics shares this task of ridge detection with many other disciplines in physics and also in other areas of research. A wealth of different approaches for the detection and segmentation of ridges has been proposed ranging from multiscale filtering (Koller et al 1995; Lindeberg 1998) and curvelet and ridgelet transforms (Starck et al 2003) to snake and watershed algorithms (Nguyen et al 2000) and combining detected ridge points by tensor voting (Medioni et al 2000). These general methods however need always be modified and optimized for specific applications. Much work in this field has been motivated by medical imaging (e.g. Jang and Hong 2002; Dimas et al 2002) and also by

[1] Max-Planck-Institut für Sonnensystemforschung, Max-Planck-Str.2, 37191 Katlenburg-Lindau, Germany E-mail: Inhester@mps.mpg.de
[2] Purple Mountain Observatory, Chinese Academy of Sciences, Nanjing, China

the application in more technical fields like fingerprint classification (Zhang and Yan 2004) and the detection of roads in areal photography (Steger 1998).

For the automated segmentation of loops a first step was made by Strous (2002, unpublished) who proposed a procedure to detect pixels in the vicinity of loops. This approach was further extended by Lee et al (2006) by means of a connection scheme which makes use of a local solar surface magnetic field estimate to obtain a prefereable connection orientation. The procedure then leads to spline curves as approximations for the loop shapes in the image. The method gave quite promizing results for artificial and also for observed trace EUV images.

The program presented here can be considered an extension of the work by Lee et al (2006). The improvements which we propose are to replace Strous' ridge point detection scheme by a modified multiscale approach of Lindeberg (1998) which automatically adjusts to varying loop thicknesses and returns also an estimate of the reliability of the ridge point location and orientation. When connecting the ridge points, we would like not to use any magnetic field information as this prejudices a later comparison of the extracted loops with field lines computed from an extrapolation of the surface magnetic field. As we consider this comparison a validity test for the underlying field extrapolation, it would be desirable to derive the loop shapes independently. Our connectivity method is therefore based only on geometrical principles which combines the orientation of the loop at the ridge point with the cocircularity constraint proposed by Parent and Zucker (1989).

The procedure is performed in three steps, each of which could be considered a module of its own and performs a very specific task. In the following chapters we explain these individual steps in some detail. In the successive chapter we apply the scheme to one of the first images observed by the SECCHI instruments on board the recently launched STEREO space craft (Howard et al 2007) in order to demonstrate the capability of our tool. Our procedure offers alternative subschemes and adaptive parameters to be adjusted to the contrast and noise level of the image to be dealt with. We discuss how the result depends the choice of some of these parameters. In a final chapter we discuss potential applications of our tool.

2 Method

Our approach consists of three modular steps, each of which is described in one of the following subsections. The first is to find points which presumably are located on the loop axis. At these positions, we also estimate the orientation of the loop for these estimates. Each item with this set of information is called a ridgel. The next step is to establish probable neighbourood relations between them which yields chains of ridgels. Finally, each chain is fitted by a smoothing spline which approximates the loop which gave rise to the ridgels.

2.1 Ridgel location and orientation

In terms of image intensities, loop structures are elongated ridge-like intensity maxima. To discriminate the maxima, we need information of the spatial derivatives of the image intensity. Commonly, these derivatives are strongly affected by image noise. In fact, numerical differentiation of data is an ill-posed problem and calls for proper regularization.

We denote by $\boldsymbol{i} \in \mathbb{I}^2$ the integer coordinate values of the pixel centres in the image and by $\boldsymbol{x} \in \mathbb{R}^2$ the 2D continuous image coordinates with $\boldsymbol{x} = \boldsymbol{i}$ at the pixel centres. We further assume that the observed image intensity $I(\boldsymbol{i})$ varies sufficiently smoothly so that a Taylor expansion at the cell centres is a good approximation to the true intensity variation $I(\boldsymbol{x})$ in the neighbourhood of $\boldsymbol{i}$, i.e.,

$$I(\boldsymbol{x}) \simeq \tilde{I}(\boldsymbol{x}) = c + \boldsymbol{g}^T(\boldsymbol{x} - \boldsymbol{i}) + (\boldsymbol{x} - \boldsymbol{i})^T \boldsymbol{H}(\boldsymbol{x} - \boldsymbol{i}) \quad (1)$$

Pixels close to a ridge in the image intensity can then be detected on the basis of the local derivatives $\boldsymbol{g}$ and $\boldsymbol{H}$ (the factor 1/2 is absorbed in $\boldsymbol{H}$). We achieve this by diagonalizing $\boldsymbol{H}$, i.e., we determine the unitary matrix $\boldsymbol{U}$ with

$$\boldsymbol{U}^T \boldsymbol{H} \boldsymbol{U} = \mathrm{diag}(h_\perp, h_\parallel) \quad \text{where} \quad \boldsymbol{U} = (\boldsymbol{u}_\perp, \boldsymbol{u}_\parallel) \quad (2)$$

where we assume that the eigenvector columns $\boldsymbol{u}_\perp$ and $\boldsymbol{u}_\parallel$ of $\boldsymbol{U}$ associated to the eigenvalues $h_\perp$ and $h_\parallel$, respectively, are ordered so that $h_\perp \le h_\parallel$.

We have implemented two ways to estimate the Taylor coefficients. The first is a local fit of (1) to the image within a $(2m+1)\times(2m+1)$ pixel box centered around each pixel $\boldsymbol{i}$:

$$(c, \boldsymbol{g}, \boldsymbol{H})(\boldsymbol{i}) = \operatorname{argmin} \sum_{\boldsymbol{j}-\boldsymbol{i}\in[-m,m]\times[-m,m]} w(\boldsymbol{i}-\boldsymbol{j}) \left(\tilde{I}(\boldsymbol{j}) - I(\boldsymbol{j})\right)^2 \tag{3}$$

We use different weight functions w with their support limited to the box size such as triangle, cos or $\cos^2$ tapers.

The second method commonly used is to calculate the Taylor coefficients (1) not from the original but from a filtered image

$$\bar{I}(\boldsymbol{x}) = \sum_{\boldsymbol{j}} w_d(\boldsymbol{x}-\boldsymbol{j}) I(\boldsymbol{j}) \tag{4}$$

As window function w_d we use a normalised Gaussian of width d. The Taylor coefficients can now be explicitly derived by differentiation of $\bar{I}$, which however acts on the window function w_d instead on the image data. We therefore effectively use a filter kernel for each Taylor coefficient which relates to the respective derivatives of the window function w_d.

One advantage of the latter method over the local fit described above is that the window width d can be chosen from $\mathbb{R}_+$ while the window size for the fit procedure must be an odd integer $2m+1$. Both the above methods regularize the Taylor coefficient estimate by the finite size of their window function. In fact, the window size could be considered as a regularization parameter.

A common problem of regularized inversions is the proper choice of the regularization parameter. Lindeberg (1998) has devised a scheme how this parameter can be optimally chosen. Our third method is a slightly modified implementation of his automated scale selection procedure. The idea is to apply method 2 above for each pixel repeatedly with increasing scales d and thereby obtain an approximation of the ridge's 2nd derivative eigenvalues $h_\perp$ and $h_\parallel$, each as a function of the scale d.

Since the $h_\perp$ and $h_\parallel$ are the principal 2nd order derivatives of the image after being filtered with w_d, they depend on the width d of the filter window roughly in the following way. As long as d is much smaller than the intrinsic width of the ridge, $d_\perp = |(\boldsymbol{u}_\perp^T \boldsymbol{\nabla})^2 \log I|^{-1/2}$, the value in $h_\perp$ will be a (noisy) estimate of the true principal 2nd derivative $(\boldsymbol{u}_\perp^T \boldsymbol{\nabla})^2 I$ of the image, independent of d. Hence, $h_\perp \propto -I_{\max}/d_\perp^2$ for $d^2 \ll d_\perp^2$. To reduce the noise and enhance the significance of the estimate, we would however like to choose d as large as possible. For $d^2 \gg d_\perp^2$, the result obtained for $h_\perp$ will reflect the shape of the window rather that of the width of the ridge, $h_\perp \propto -\bar{I}_{\max}/d^2 = -I_{\max} d_\perp / d^3$ for $d^2 \gg d_\perp^2$. Roughly, details near $d \sim d_\perp$ depend on the exact shape of the ridge, we have

$$h_\perp(d) \sim \frac{-d_\perp}{\left(d_\perp^2 + d^2\right)^{3/2}} \tag{5}$$

For each pixel we consider in addition a quality function

$$q(d) = d^\gamma (|h_\perp| - |h_\parallel|) \ , \quad \gamma \in (0,3) \tag{6}$$

which will vary as d^γ for small d and drop asymptotically to zero for $d \gg d_\perp$ as $d^{\gamma-3}$. In between, $q(d)$ will reach a maximum approximately where the window width d matches the local width $d_\perp$ of the ridge (which is smaller than the scale along the ridge). The choice of the right width d has now been replaced by a choice for the exponent γ. The result, however, is much less sensitive to variations in γ. Smaller values of γ shift the maximum of q to slightly smaller values of d and hence tend to favour more narrow loop structures. While γ is a constant for the whole image in this automated scale selection scheme, the window width d and the finally adopted Taylor coefficients are chosen individually for every pixel from the respective maximum of the quality factor q.

In Fig. 1 we show as an example a λ=171Å image of active region NOAA 10930 observed by SECCHI/STEREO at 2007-12-12 20:43 UT and the corresponding image of q obtained with $\gamma = 0.75$ and window sizes d in the range of 0.6 to 4 pixels. Clearly, the q factor maximizes in the vicinity of the loops. The distribution of the scales d for which the maximum q was found for each pixel is shown in Fig. 2. About 1/3 of the pixels had optimal widths < 1 pixel, many of which originate from local longated noise and moss features of the image. The EUV moss are amorphous emissions which

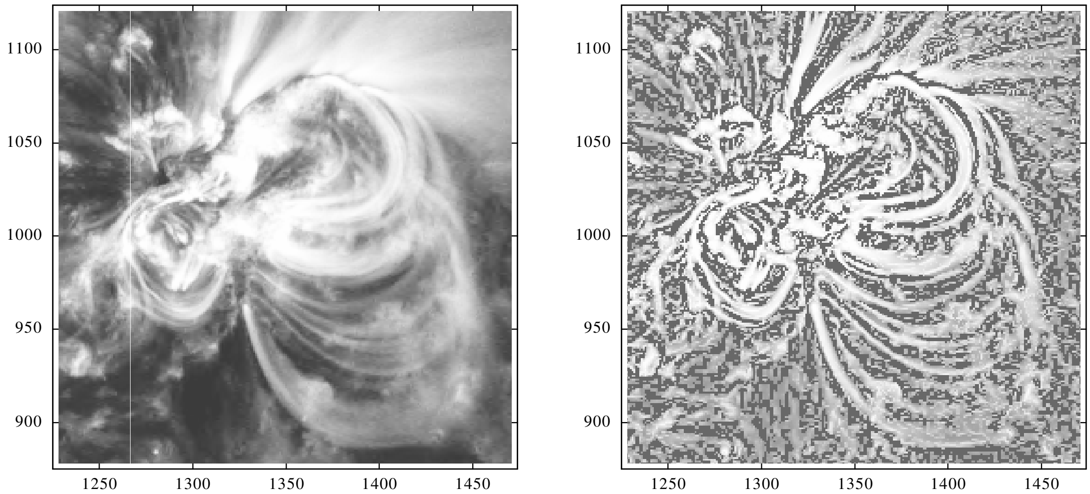

Fig. 1 Original image of active region NOAA 10930 observed by SECCHI/STEREO (left) and the corresponding image of the quality factor q (6) obained from the third ridgel determination method by automated scale selection (right). This image was taken at $\lambda = 171$Å on 2006-12-12 20:43 UT and was not processed by the SECCHI_prep routine.

originate in the upper transition region Berger et al (1999) and are not associated with loops. For proper loop structures the optimum width found was about 1.5 pixels with, however a widely spread distribution.

In the case that $\boldsymbol{i}$ is located exactly on a ridge, $\boldsymbol{u}_\perp$ is the direction across and $\boldsymbol{u}_\parallel$ the direction along the ridge and $h_\perp$ and $h_\parallel$ are the associated second derivatives of the image intensity in the respective direction. A positive ridge is the identified from the Taylor coefficients by means of the following conditions (Lindeberg 1998)

$$\boldsymbol{u}_\perp^T \boldsymbol{\nabla} I = \boldsymbol{u}_\perp^T \boldsymbol{g} = 0 \quad \text{a vanishing gradient cross the ridge} \tag{7}$$

$$(\boldsymbol{u}_\perp^T \boldsymbol{\nabla})^2 I = h_\perp < 0 \quad \text{a negative 2nd order derivative across the ridge} \tag{8}$$

$$|(\boldsymbol{u}_\perp^T \boldsymbol{\nabla})^2 I| > |(\boldsymbol{u}_\parallel^T \boldsymbol{\nabla})^2 I| \text{ or } |h_\perp| > |h_\parallel| \quad \text{a 2nd order derivative magnitude across the} \tag{9}$$

$$\text{ridge larger than along} \tag{10}$$

The latter two inequalities are assumed to also hold in the near neighbourhood of the ridge and are used to indicate whether the pixel centre is close to a ridge.

In the vicinity of the ridge, along a line $\boldsymbol{x} = \boldsymbol{i} + \boldsymbol{u}_\perp t$, the image intensity (1) then varies as

$$I(t) \simeq c + \boldsymbol{u}_\perp^T \boldsymbol{g} t + \boldsymbol{u}_\perp^T \boldsymbol{u}_\perp h_\perp t^2 \tag{11}$$

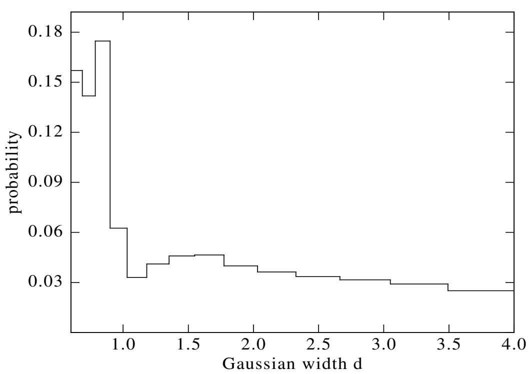

Fig. 2 Distribution of withs d of the window function w_d for which (6) was found to maximize for the data in (1). The maximum was determined for each image pixel for which $h_\perp < |h_\parallel|$.

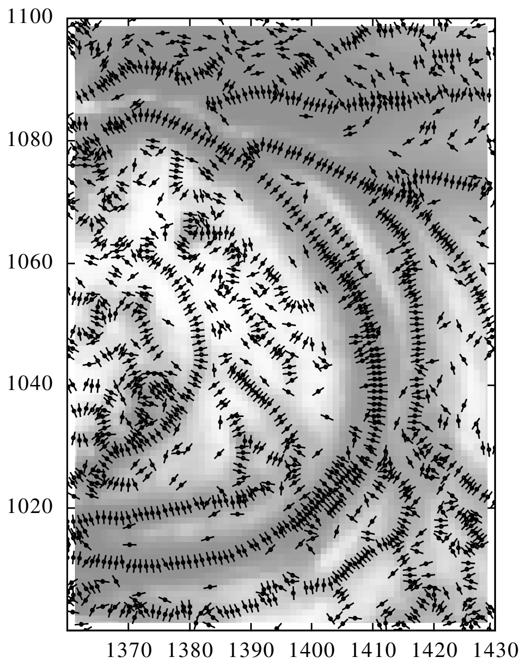

Fig. 3 Comparison of the resulting ridgels from interpolation method (13, left) and (14, right). The images show an enlarged portion of the original data in Fig. 1. The short sticks denote the local orientation of $\boldsymbol{u}_\perp$ on the loop trace.)

According to the first ridge criterium (7), the precise ridge position is where $I(t)$ has its maximum. Hence the distance to the ridge is

$$t_{\max} = -\frac{\boldsymbol{u}_\perp^T \boldsymbol{g}}{2h_\perp \boldsymbol{u}_\perp^T \boldsymbol{u}_\perp} \tag{12}$$

and a tangent section to the actual ridge curve closest to $\boldsymbol{i}$ is

$$\boldsymbol{r}(s) = \boldsymbol{i} - \frac{\boldsymbol{u}_\perp \boldsymbol{u}_\perp^T \boldsymbol{g}}{2h_\perp \boldsymbol{u}_\perp^T \boldsymbol{u}_\perp} + s\boldsymbol{u}_\parallel \quad \text{for} \quad s \in \mathbb{R} \tag{13}$$

Note that $\boldsymbol{u}_\perp^T \boldsymbol{u}_\perp = 1$ for a unitary $\boldsymbol{U}$.

We have implemented two methods for the interpolation of the ridge position from the Taylor coefficients calculated at the pixel centres. One is the interpolation of the ridge centre with the help of (13). The second method interpolates the zeros of $\boldsymbol{u}_\perp^T \boldsymbol{g}$ in between neighbouring pixel centres $\boldsymbol{i}$ and $\boldsymbol{j}$ if its sign changes. Hence the alternative realization of (7) is

$$\begin{aligned} &\text{if} \quad |c| = |\boldsymbol{u}_\perp^T(\boldsymbol{i})\boldsymbol{u}_\perp(\boldsymbol{j})| > c_{\min} \\ &\text{and} \quad \operatorname{sign}(c)(\boldsymbol{u}_\perp^T\boldsymbol{g})(\boldsymbol{j})\ (\boldsymbol{u}_\perp^T\boldsymbol{g})(\boldsymbol{i}) < 0 \quad \text{then} \end{aligned}$$

$$\boldsymbol{r} = \boldsymbol{i} + t(\boldsymbol{j} - \boldsymbol{i}) \tag{14}$$

$$\text{where} \quad t = \frac{(\boldsymbol{g}^T\boldsymbol{u}_\perp)(\boldsymbol{i})}{(\boldsymbol{g}^T\boldsymbol{u}_\perp)(\boldsymbol{i}) - \operatorname{sign}(c)(\boldsymbol{g}^T\boldsymbol{u}_\perp)(\boldsymbol{j})}$$

The first condition insures that $\boldsymbol{u}_\perp(\boldsymbol{i})$ and $\boldsymbol{u}_\perp(\boldsymbol{j})$ are sufficiently parallel or antiparallel. Note that the orientation of $\boldsymbol{u}_\perp$ of neighbouring pixels may be parallel or antiparallel because an eigenvector $\boldsymbol{u}_\perp$ has no uniquely defined sign.

In general, the interpolation according to (13) yields fewer ridge points along a loop but they have a fairly constant relative distance. With the second method (14), the ridge points can only be found at the intersections of the ridge with the grid lines connecting the pixel centres. For ridges directed

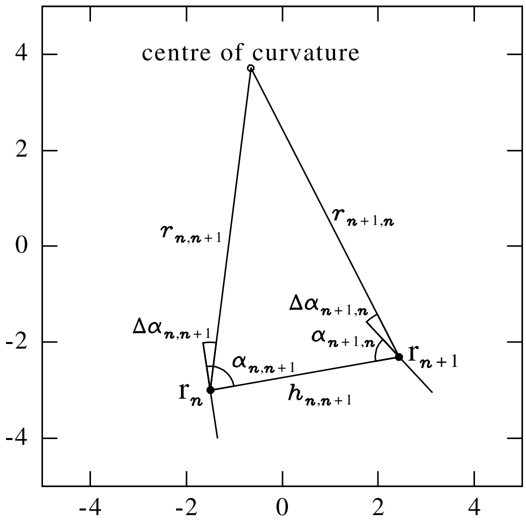

Fig. 4 Illustration of angles and distances of a connection element between two ridgels according to the cocircularity condition of Parent and Zucker (1989). The ridgel positions are indicated by a small full dot, the ridge normal orientation by the line centred at the ridgel position.

obliquely to the grid, the distances between neighbouring ridge points produced may vary by some amount. Another disadvantage of the second method is that it cannot detect faint ridges which are just about one pixel wide. It needs at least two detected pixels neighbouring in direction across the ridge to properly interpolate the precise ridge position. The advantage of the second method is that it does not make use of the 2nd order derivative $h_\perp$ which unavoidably is more noisy than the 1st order derivative $\boldsymbol{g}$. In Fig. 3 we compare the ridgels obtained wth the two interpolation methods for the same image.

The final implementation of identifying ridge points in the image comprises two steps: First the Taylor coefficients (1) are determined for every pixel and saved for those pixels which have an intensity above a threshold value $I_{\min}$, for which the ridge shape factor $(h_\perp^2 - h_\parallel^2)/(h_\perp^2 + h_\parallel^2)$ exceeds a threshold $s_{\min}$ in accordance with(10) and which also satisfy (8). The second step is then to interpolate the precise sub-pixel ridge point position from the derivatives at these pixel centres by either of the above methodes. This interpolation complies with the 3rd ridge criterium (7). The ridgel orientation $\boldsymbol{u}_\perp$ are also interpolated from the cell centres to the ridgel position. The information retained for every ridge point n in the end consists of its location $\boldsymbol{r}_n$, and the ridge normal orientation $\boldsymbol{u}_{\perp,n}$ defined modulo π.

2.2 Ridgel connection to chains

The basics for the connection of ridgels is the cocircularity condition of Parent and Zucker (1989).

For two ridgels at $\boldsymbol{r}_n$ and $\boldsymbol{r}_{n+1}$ a virtual centre of curvature can be defined which forms an isosceles triangle with the ridgels as shown in Fig. 4. One edge is formed by the connection between the two ridgels of mutual distance $h_{n,n+1}$. The two other triangle edges in this construction connect one of the two ridgels with the centre of curvature which is chosen so that these two symmetric edges of the isosceles triangle make angles $\Delta\alpha_{n,n+1}$ and $\Delta\alpha_{n+1,n}$ as small as possible with the respective ridgel orientation $\boldsymbol{u}_{\perp,n}$ and $\boldsymbol{u}_{\perp,n+1}$, respectively. It can be shown that

$$\min\,(\Delta\alpha_{n,n+1}^2 + \Delta\alpha_{n+1,n}^2)$$

requires equal magnitudes for the angles $\Delta\alpha_{n,n+1}$ and $\Delta\alpha_{n+1,n}$. The distance $r_{n,n+1} = r_{n+1,n}$ is the local curvature radius and can be calculated from

$$r_{n,n+1} = r_{n+1,n} = \frac{\frac{1}{2}h_{n,n+1}}{\cos\left(\frac{1}{2}(\alpha_{n,n+1} + \alpha_{n+1,n})\right)} \tag{15}$$

where $\alpha_{n,n+1}$ is the angle between $\boldsymbol{r}_{n+1} - \boldsymbol{r}_n$ and $\pm\boldsymbol{u}_{\perp,n}$, the sign being chosen so that $|\alpha_{n,n+1}| < \pi/2$.

With each connection between a pair of ridgels we associate a binding energy which depends on the parameters derived above in the form:

$$e_{n,n+1} = \Big(\frac{\Delta\alpha_{n,n+1}}{\alpha_{\max}}\Big)^2 + \Big(\frac{r_{\min}}{r_{n,n+1}}\Big)^2 + \Big(\frac{h_{n,n+1}}{h_{\max}}\Big)^2 - 3 \tag{16}$$

Note that $\Delta\alpha^2_{n,n+1} = \Delta\alpha^2_{n+1,n}$ according to the cocircularity construction and hence $e_{n,n+1}$ is symmetric in its indices. The three terms measure three different types of distortions and can be looked upon as the energy of an elastic line element. The first term measures the deviation of the ridgel orientation from strict cocircularity, the second the bending of the line element, the third term its stretching. The constants $\alpha_{\max}$, $r_{\min}$ and $h_{\max}$ give us control on the relative weight of the three terms. $r_{\min}$, e.g., is the smallest acceptable curvature radius, $h_{\max}$ the largest acceptable distance if we only accept connections with a negative value for the energy (16).

In practical applications, the energy (16) is problematic since it puts nearby ridgel pairs with small distances $h_{n,n+1}$ in a severe disadvantage because small changes of their $\boldsymbol{u}_\perp$ easily reduces on the curvature radius $r_{n,n+1}$ below acceptable values. We therefore allow for measurement errors in $\boldsymbol{r}$ and $\boldsymbol{u}_\perp$ and the final energy considered is the minimum of (16) within these given error bounds.

The final goal is to establish a whole set of connections between as many ridgels as possible so that the the individual connections add up to chains. Note that each ridgel has two "sides" and we only allow at most one connection on either side to its orientation defined by $\boldsymbol{u}_\perp$. This restriction avoids junctions in the chains we are going to generate. The sum of the binding energies (16) of all accepted connections ideally should attain a global minimum in the sense that any alternative set of connections which complies with the above restriction should yield a larger energy sum.

We use the following approach to find a state which comes close to this global minimum. The energy $e_{n,n+1}$ is calculated for each ridgel pair less than $h_{\max}$ apart and those connections which have a negative binding energy are stored. These latter are the only connections which we expect to contribute to the energy minimum. Next we order the stored connections according to their energy and connect the ridgels to chains starting from the lowest energy connection. Connections to one side of a ridgel which has already been occupied by a lower energy connection before are simply discarded.

2.3 Curve fits to the ridgel chains

In this final section we calculate a smooth fit to the chains of ridgels obtained above. The fit curve should level out small errors in the position and orientation of individual ridgels. We found from experiments that higher order splines functions are far too flexible for the curves we aim at. We expect that magnetic field lines in the corona do not rapidly vary their curvature along their length and we assume this also holds for their projections on EUV images. We found that parametric polynomes of 3^{rd} or 5^{th} degree are sufficient for our purposes. Hence for each chain of ridgels we seek polynomial coefficients $\boldsymbol{q}_n$ which generate a two-dimensional curve

$$\boldsymbol{p}(t) = \sum_{n=0}^{5} \boldsymbol{q}_n t^n \quad \text{for} \quad t \in [-1, 1] \tag{17}$$

which best approximates the chain of ridgels. What we mean by "best approximation" will be defined more precisely below. The relevant parameters of this approximation are sketched in Fig. 5.

The polynomial coefficients $\boldsymbol{q}$ of a fit (17) are determined by minimising

$$\sum_{i \in \text{chain}} (\boldsymbol{d}_i^T \boldsymbol{d}_i) + \mu(\boldsymbol{p}''^T \boldsymbol{p}'')(t_i) \tag{18}$$
$$\text{where} \quad \boldsymbol{d}_i = \boldsymbol{r}_i - \boldsymbol{p}(t_i)$$

with respect to $\boldsymbol{q}_n$ for a given μ. Initially, we distribute the curve parameters t_i in the interval $[-1, 1]$ such that the differences $t_i - t_j$ of neighbouring ridgels are proportional to the geometric distances $|\boldsymbol{r}_i - \boldsymbol{r}_j|$. The $\boldsymbol{p}''$ are the second order derivative of (17). Hence, the second term increases with increasing

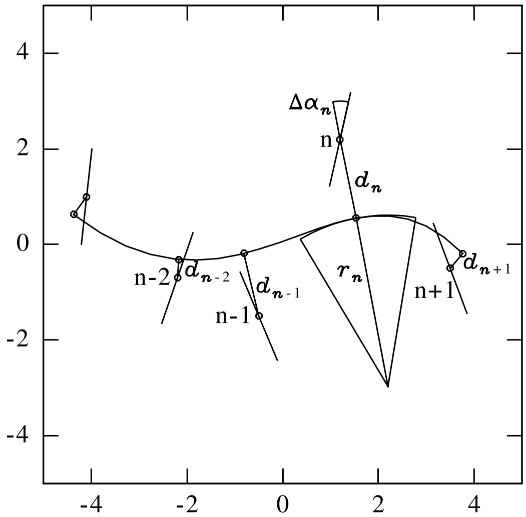

Fig. 5 Sketch of the curve fit parameters. The ridgels are represented by their location and the two pixel long bar of the rpc orientation. For each ridgel i, the proximity to the smooth fit curve is expressed by their distance d_i and the angle $\Delta\alpha_i$ between the distance direction of $\boldsymbol{d}_i$ to the curve and the rpc orientation. Another measure of the quality of the curve is the inverse curvature radius r.

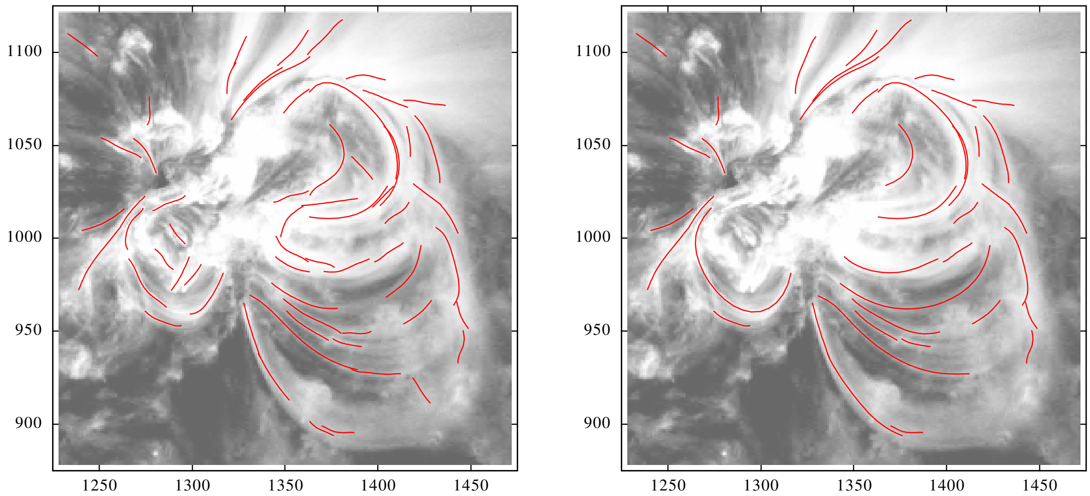

Fig. 6 Fit curves obtained for those chains which involve 10 or more ridgels (left) and curves remaining after cleaning of those curves which are due to moss (right).

curvature of the fit while a more strongly curved fit is required to reduce the distances $\boldsymbol{d}_i$ between $\boldsymbol{r}_i$ and the first order closest curve point $\boldsymbol{p}(t_i)$.

The minimum coefficients $\boldsymbol{q}_n(\mu)$ can be found analytically in a straight forward way. Whenever a new set of $\boldsymbol{q}_n(\mu)$ has been calculated, the curve nodes t_i are readjusted by

$$t_i = \mathrm{argmin}_t (\boldsymbol{r}_i - \boldsymbol{p}(t))^2 \tag{19}$$

so that $\boldsymbol{p}(t_i)$ is always the point along the curve closest to the ridgel.

For different μ this minimum yields fit curves with different levels of curvature. The local inverse curvature radius can at any point along the curve be calculated from (17) by

$$\frac{1}{r(t)} = \frac{|\boldsymbol{p}''(t) \times \boldsymbol{p}'(t)|}{|\boldsymbol{p}'(t)|^3} \tag{20}$$

The final μ is then chosen so that

$$E_{\text{chain}}(\mu) = \sum_{i\in\text{chain}} \frac{d_i^2}{d_{\max}^2} + \sum_{i\in\text{chain}} \frac{\Delta\alpha_i^2}{\alpha_{\max}^2} + r_{\min}^2 \int_{-1}^{1} \frac{1}{r(t)^2}\, dt \tag{21}$$

is a minimum where $\Delta\alpha_n$ is the angle between the local normal direction of $\boldsymbol{d}_n$ of the fit curve and the ridgel orientation $\pm\boldsymbol{u}_{\perp,n}$, the sign again chosen to yield the smallest possible $|\Delta\alpha_i|$ The meaning of the terms is obvious and clearly the first two terms in general require a large curvature which is limited by the minimization of the last term.

Expression (21) depends nonlinearly on the parameter μ which we use to controll the overall curvature. The minmum for (21) is found by iterating μ starting from a large numerical value, i.e., a straight line fit. The parameters $r_{\min}$, $\alpha_{\max}$ and $d_{\max}$ can be used to obtain fits with a different balance between the mean square spatial and angular deviation of the fit form the "observed" chain of ridgels and the curvature of the fit. Unless these parameters are chosen reasonably, e.g. $r_{\min}$ not too small, we have always found a minimum for (21) after a few iteration steps.

In the left part of Fig. 6 we show the final fits obtained. For this result, the ridgels were found by automated scaling and interpolated by method (13), the parameters in (16) and (21) were $h_{\max} = 3.0$ pixels $r_{\min} = 15.0$ pixels and $a_{\max} = 10.0$ degrees. The fits are represented by 5^{th} degree parametric polynomials.

Obviously, the image processing cannot easily distinguish between structures which are due to moss and bright surface features and coronal loops. Even the observer is sometimes misled and there are no rigorous criteria for this distinction. Roughtly, coronal loops produce longer and smoother fit curves, but there is no strict threshold because it may appear that the fit curve is split along a loop where the loop signal becomes faint. As a rule of thumb, a restriction to smaller curvature by choosing a higher parameter $r_{\max}$ and discarding shorter fit curves tends to favour coronal loops. Eventually, however, also loops are suppressed. We have therefore appended a user interactive tool as the last step of our processing which allows to eliminate unwanted curves, merge or split curves when smooth fits result with an energy (21) of the output fits not much higher than the energy of the input. The left part of Fig. 6 shows the result of such a clearing step.

3 Application

In this section we present an application of our segmentation tool to another EUV image of active region NOAA 10930 taken by the SECCHI/STEREO A instrument. This EUV image was observed at λ =195Å on 2006-12-12 23:43:11 UT and was processed by the IDL program SECCHI_prep (see `http://secchi.nrl.navy.mil/wiki/pmwiki.php?n=Main.SecchiPrepFeatureRequests`) At that time the STEREO spacecrafts still were close so that stereoscopy could not be applied. We therefore selected an image which was taken close to the MDI magnetogram observed at 23:43:30 UT on the same day. It is therefore possible to calculate magnetic field lines from an extrapolation model and project them into the STEREO view direction to compare them with the loop fits obtained with our tool. In Fig. 7 the MDI contour lines of the line of sight field strength were superposed on the EUV image.

The loop fits here were obtained by applying the automated scaling with d up to 2 pixels, i.e. window sizes up to $2d + 1 = 5$ pixels, to identify the ridgels. Pixels with maximum quality q below 0.4 were discarded and we applied method (13) to interpolate the local ridge maxima. $h_{\max} = 5.0$ pixels, $r_{\min} = 15.0$ pixels and $a_{\max} = 10.0$ degrees. The fits are 5^{th} degree parametric polynomials. In Fig. 8, we show some of the fits obtained which are most likely associated with a coronal loop. They are superposed onto the EUV image as red lines. Those loops which were found close to computed magnetic field lines are displayed again in the left part of Fig. 9 with loop numbers so that they can be identified.

The magnetic field lines were computed from the MDI data by extrapolation based on a linear force-free field model (see Seehafer 1978; Alissandrakis 1981, for details). This model is a simplification of the general nonlinear force-free magnetic field model

$$\nabla \times \mathbf{B} = \alpha\mathbf{B} \quad \text{where} \quad \mathbf{B}\cdot\nabla\alpha = 0$$

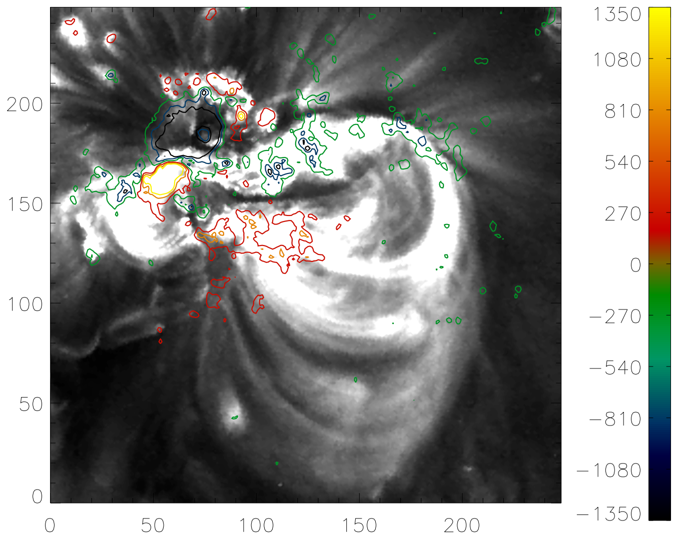

Fig. 7 MDI contours overlaid on the SECCHI/STEREO EUV image for NOAA 10930. The EUV and MDI data were recorded on 12 December 2006 at 23:43:11 UT and 23:43:30 UT, respectively. The colour cose on the right indicates the field strength at the coutour lines in Gauss.

and α may vary on different field lines. An extrapolation of magnetic surface observations based on this model requires boundary data from a vector magnetograph. The linear force-free field model treats α as a global constant. The advantage of linear force-free field model is that it requires only a line-of-sight magnetogram, such as MDI data, as input.

A test of the validity of the linear forec-free assumption is to determine different values of α from a comparison of field lines with individual observed loop structures (e.g. Carcedo et al 2003)). The range of α obtained then indicates how close the magnetic field can be described by the linear model. Since the linear force-free field has the minimum energy for given normal magnetic boundary field and magnetic helicity, a linear force-free field is supposed to be much more stable than the more general non-linear field configuration (Taylor 1974).

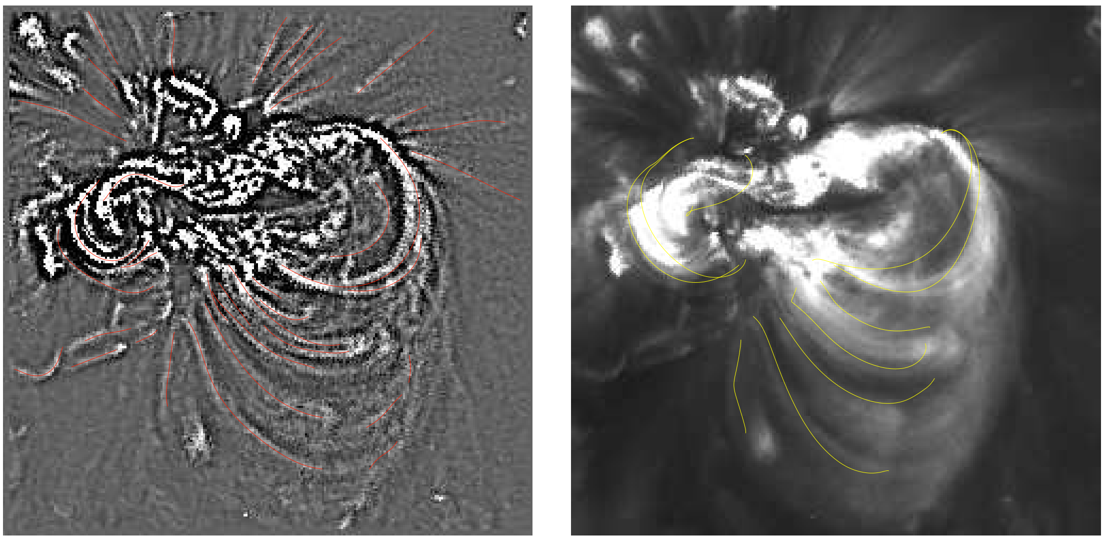

Fig. 8 The left diagram shows as red lines the loops identified by the segmentation tool for the EUV image in Fig. 7. In order to show the loops more clearly, the image in the background was contrast enhanced by an unsharp mask filter. The right diagram displays in yellow field lines calculated from the MDI data. The fieldlines were selected so that they are located closest to the extracted loops in the left part of the image. See the text for more details on how the field lines were determined.

Table 1 Identified loops, α values of the best fitting field lines and the averaged distances in units of pixel between the loop and the best fitting field line.

Loop No.	C_l(b)(pixel)	$\alpha(10^{-3}Mm^{-1})$
1	3.19569	-10.6800
3	3.75232	-35.6000
4	2.34320	-9.25600
11	10.7692	-35.6000
13	0.48639	2.13600
14	1.36359	-9.25600
15	4.23864	17.0880
17	4.89116	16.3760
18	2.42555	-14.2400
19	2.53884	-32.7520

We calculated about 5000 field lines with the linear force-free model with the α value varied in the range from -0.0427Mm^{-1} to 0.0356Mm^{-1}. These field lines were then projected onto the EUV image for a comparison with the detected loops.

For each coronal loop l_i, we calculate the average distance of the loop to every projected field line b_j discarding those field lines which do not fully cover the observed loop l_i. This distance is denoted by $C_{l_i}(b_j)$. For details of this distance calculation see Feng et al (2007). In the end we could find a closest field line for every coronal loop by minimizing $C_{l_i}(b_j)$. The detected loops and their closest field lines are plotted in the right diagram of Fig. 9 An overplot of the closest field lines onto the EUV image is shown in Fig.8

In Table 1 we list the distance measure C along with the loop number and the linear force-free parameter α for the closest field line found. We find that our α values are not uniform over this active region, that is, the linear force-free model is not adequate to describe the magnetic properties of this active region. This is also seen by the characteristic deviation at their the upper right end in Fig. 8 between the eastwards inclined loops (solid) and their closest projected field lines (dotted). With no value of α the shape of these loops could be satisfactorily fitted. Further evidence for strong and inhomogeneous currents in the active region loops is provided by the fact that only 2.5 hours later, at 02:14 UT on 13 December, a flare occurred in this active region and involved the magnetic structures associated with loops 2, 4 and 17.

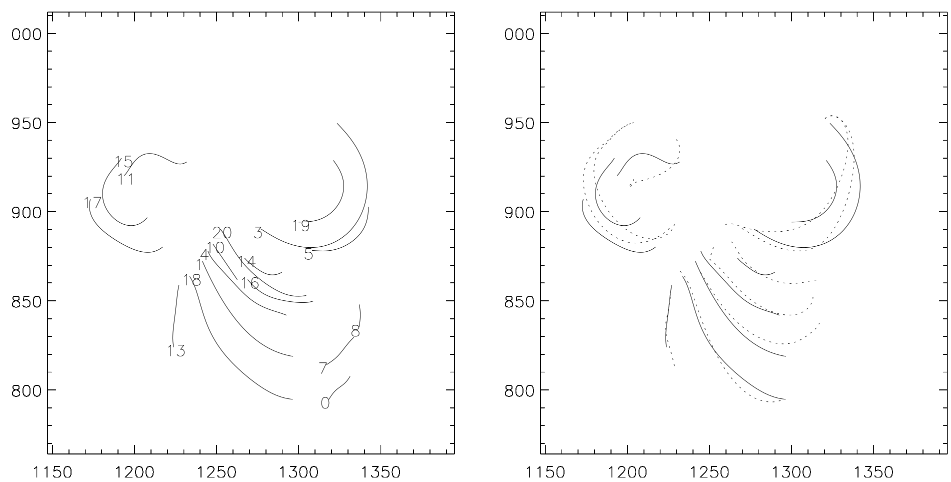

Fig. 9 The left panel shows the loops identified by the segmentation tool which correspond to the closed magnetic filed lines; In the right panel are the loops (solid lines) with their best fitting field lines(dotted lines). x and y axis are in units of EUV pixel.

4 Discussion

EUV images display a wealth of structures and there is a strong need to reduce this information for specified analyses. For the study of the coronal magnetic field, the extraction of loops from EUV images is a particularly important task. Our tool intends to improve earlier work in this direction. Whether we have achieved this goal can only be decided from a rigourous comparison which is underway elsewhere (Aschwanden et al 2007). At least from a methodological point of view we expect that our tool should yield improved results compared to Strous (2002, unpublished) and Lee et al (2006).

From the EUV image alone it is often difficult to decide which of the features are associated with coronal loops and which are due to moss or other bright surface structures. A final comparison of the loops with the extrapolated magnetic field and its field line shapes is therefore very helpful for this distinction. Yet we have avoided to involve the magnetic field information in the segmentation procedure which extracts the the loops from the EUV image because this might bias the loop shapes obtained.

For the case we have investigated, we find a notable variation of the optimal α values and also characteristic deviation of the loop shapes from the calculated field lines. These differences are evidence of the fact that the true coronal magnetic field near this active region is not close to a linear force-free state. This is in agreement with earlier findings. Wiegelmann et al (2005), e.g., have shown for another active region that a nonlinear force-free model describes the coronal magnetic field more accurately than linear models. The computation of nonlinear models is, however, more involved due to the nonlinearity of the mathematical equations (e.g. Wiegelmann 2004; Inhester and Wiegelmann 2006). Furthermore, these models require photospheric vector magnetograms as input, which were not available for the active region investigated.

Coronal loops systems are often very complex. In order to acess them in 3D, the new SECCHI/STEREO telescopes now provides EUV images which can be analysed with stereoscopic tools. We plan to apply our loop extraction program to EUV images from different viewpoints and undertake a stereoscopic reconstruction of the true 3D structure of coronal loops along the lines described by Inhester (2006) and Feng et al (2007). The knowledge of the 3D geometry of a loop allows to estimate more precisely its local EUV emissivity. From this quantity we hope to be able to derive more reliably the plasma parameters along the length of the loop.

Other applications can be envisaged. An interesting application of our tool, e.g., will be the investigaetion of loop oscillations. Here, the segmentation tool will be applied to times series of EUV images. We are confident that oscillation modes and in case of a SECCHI/STEREO pairwise image sequence also the polarisation of the loop oscillation can be discerned.

5 Acknowledgement

The authors thank the MDI/SOHO and the SECCHI/STEREO consortia for the supply of their data. SOHO and STEREO are a joint projects of ESA and NASA. BI thanks the International Space Institute, Bern, for their hospitality and the head of its STEREO working group, Thierry DuDdoc de Wit and also Jean-Francois Hochedez for stimulating discussions. LF was supported by the IMPRESS graduate school run jointly by the Max Planck Society and the Universities Göttingen and Braunschweig. The work was furthermore supported by DLR grant 50OC0501.

References

Alissandrakis CE (1981) On the computation of constant alpha force-free magnetic field. A&A 100:197–200

Aschwanden M, Gary GA, Smith M, Inhester B, Schrijver K, DeRosa M (2007) Automated tracing of coronal loops. in preparation for Solar Physics

Berger T, De Pontieu B, Fletcher L, Schrijver C, Tarbell T, Title A (1999) What is moss. Solar Physics 190:409–418

Carcedo L, Brown DS, Hood AW, Neukirch T, Wiegelmann T (2003) A Quantitative Method to Optimise Magnetic Field Line Fitting of Observed Coronal Loops. Sol Phys 218:29–40

Dimas A, Scholz M, Obermayer K (2002) Automatic segmentation and skeletonization of neurons from confocal microscopy images based on the 3d wavelet transform. IEEE Transactions on Image Processing 11(7):790–801

Feng L, Wiegelmann T, Inhester B, Solanki S, Gan W, Ruan P (2007) Magnetic stereoscopy of coronal loops in noaa8891. accepted for publication in Solar Physics
Howard R, et al (2007) Secchi instrument description. in preparation
Inhester B (2006) Stereoscopy basics for the STEREO mission. To appear as an ISSI publication, available at ArXiv Astrophysics e-prints astro-ph/0612649
Inhester B, Wiegelmann T (2006) Nonlinear Force-Free Magnetic Field Extrapolations: Comparison of the Grad Rubin and Wheatland Sturrock Roumeliotis Algorithm. Sol Phys 235:201–221
Jang JH, Hong KS (2002) Detection of curvilinear structures and reconstruction of their regions in grey scale images. Pattern Recognition 35:807–824
Koller T, Gerig B, Szkely G, Dettwiler D (1995) Multiscale detection of curvilinear structures in 2-d and 3-d image data. In: Proceedings Fifth Int. Conf. on Computer Vision (ICCV95), IEEE Computer Society Press, pp 864–869
Lee JK, Newman TS, Gary GA (2006) Oriented connectivity-based method for segmenting solar loops. Pattern Recognition 39:246–259
Lindeberg T (1998) Edge detection and ridge detection with automatic scale selection. International Journal of Computer Vision 30(2):117–154
Medioni G, Tang CK, Lee MS (2000) Tensor voting: Theory and applications. URL citeseer.ist.psu.edu/-medioni00tensor.html
Nguyen H, Worring M, van den Boomgaard R (2000) Watersnakes: Energy-driven watershed segmentation. URL citeseer.ist.psu.edu/article/nguyen00watersnakes.html
Parent P, Zucker S (1989) Trace inference, curvature consistency and curve detection. IEEE Transactions on Pattern Analysis and Machine Intelligence 11:823–839
Seehafer N (1978) Determination of constant alpha force-free solar magnetic fields from magnetograph data. Sol Phys 58:215–223
Starck JL, Donoho DL, Candès EJ (2003) Astronomical image representation by the curvelet transform. Astronomy and Astrophysics 398:785–800
Steger C (1998) An unbiased detector of curvilinear structures. IEEE Transactions on Pattern Analysis and Machine Intelligence 20(2):113–125
Taylor JB (1974) Relaxation of Toroidal Plasma and Generation of Reverse Magnetic Fields. Physical Review Letters 33:1139–1141
Wiegelmann T (2004) Optimization code with weighting function for the reconstruction of coronal magnetic fields. Sol Phys 219:87–108
Wiegelmann T, Lagg A, Solanki SK, Inhester B, Woch J (2005) Comparing magnetic field extrapolations with measurements of magnetic loops. A&A 433:701–705
Zhang Q, Yan H (2004) Fingerprint classification based on extraction and analysis of singularities and pseudo ridges. Pattern Recognition 37:2233–2243